Supporting Information

Assembly of β–$Cu_2V_2O_7$ /WO_3 heterostructured nanocomposites and the impact of their composition-dependent structure on the photoelectrochemical properties.

Mariateresa Scarongella[+a], Chethana Gadiyar[+a], Michal Strach[a], Luca Rimoldi[b], Anna Loiudice[a], Raffaella Buonsanti[a*]

a. Laboratory of nanochemistry for energy, Institute of Chemical Sciences and Engineering, EPFL, Sion, 1050, Switzerland
b. Department of Chemistry, Università degli Studi di Milano, 20133 Milan, Italy

+ These authors have contributed equally to the work.

*email: raffaella.buonsanti@epfl.ch

EXPERIMENTAL Details

Materials
Copper (I) acetate (CuOAc, 97%), hexane (anhydrous, 95%) was purchased from TCI Deutschland GmbH. Sodium hydroxide (NaOH, 97%), Toluene (anhydrous), Dimethylformamide (DMF, anhydrous) and Acetonitrile (ACN, anhydrous) were purchased from abcr GmbH. Oleic acid (OLAC,), Oleylamine (OLAM, 70%), Vanadyl acetylacetonate ($VO(acac)_2$, 98%) , Trioctylamine (TOA, 98%), tetradecylphosphonic acid (TDPA, 97%), trimethyloxonium tetrafluoroborate (Me_3OBF_4, 95%), sodium sulphite (Na_2SO_3, 98%) and ethanol (anhydrous) were purchased from Sigma-Aldrich and used as received. Boric acid (H_3BO_3, 99.8%) was purchased from ROTH AG.

Synthesis of the Cu nanocrystals (NCs).
6nm Cu NCs were synthesized by modifying the procedure from Hung et al.[1] 10 mL of TOA was introduced into a three-necked flask and kept under vacuum for 30 min. This step was followed by heating under nitrogen flow at 130°C for 30 minutes. Following the cooling of TOA to room temperature, 1 mmol of CuOAc and 0.5 mmol of TDPA were added to the flask under vigorous stirring. The solution was then heated to 180°C and maintained at this temperature for 30 minutes followed by one final heating step to 300°C for 30 minutes. The solution was naturally cooled to 60°C and transferred to a vial under N_2 flow. Anhydrous ethanol was added for washing and the solution centrifuged at 6000 rpm for 20 minutes. The precipitate was dispersed in hexane and kept under N_2 in glovebox.

Synthesis of WO_3 nanorods (NRs).
WO_3 nanorod synthesis was conducted by following a procedure previously reported by Loiudice et al.[2,3] Briefly, 5.3 mL of OLAC were added to a 3-neck flask together with 1.8 mL of OLAM and 100 mg of WCl_4. The mixture was heated under the nitrogen flow to 300°C. The mixture was maintained at 300°C for 2 hours while stirring and then cooled to room temperature. Successively, the obtained colloidal solution was washed in acetone several times by centrifugation/resuspension cycles (15 min each, 3800 rpm) adopting 0.5 mL toluene for resuspension. The solution was finally dispersed in hexane.

Ligand stripping of Cu NCs and WO_3 NRs.
In order to make a homogeneous solution in DMF of Cu NCs, WO_3 NRs and $VO(acac)_2$ the native ligands of the Cu NCs and WO_3 NRs need to be removed. The ligand stripping was performed following our established procedure.[4] Firstly, the concentration of the nanocrystal solutions was determined by ICP-OES. Then, 1 mL of a solution 0.05 M of the as-synthesized Cu NCs (or WO_3 NRs) in hexane was added to a solution of 50 mg of Me_3OBF_4 in 1 mL of ACN and vigorously stirred

for 3 minutes. 1 mL of toluene was added to the solution followed by centrifugation at 6000 rpm for 15 minutes. The precipitate was dispersed in 250 μL of DMF. The above procedure was performed in a glove box for Cu NCs and in air for WO_3 NRs.

Inductively-Coupled-Plasma Optical Emission Spectroscopy (ICP-OES).
ICP-OES was performed on Agilent 5100 model to determine the Cu, V and W concentration. 5 standard solutions of Cu, V and W were prepared to obtain the calibration curve used to determine the concentrations of the digested solution and films. For the solutions, upon evaporation of the hexane, 285 μl of 70% HNO_3 was added to 20 μl of the as-synthesized Cu NC or WO_3 NR solutions and left overnight to ensure complete digestion of the samples. Following this step, 9.715 mL of Millipore water was added to the solution to reach the 2% acid content needed for the analysis. The nanocomposite films were digested in 500 μl of 70% HNO_3 and the solution left overnight for complete dissolution of the film. The solution was further diluted to 2% HNO_3 for analysis using ICP-OES to determine the concentration of Cu, V and W.

Synthesis of nanocrystalline β–$Cu_2V_2O_7$ (CVO) thin films.
The preparation of nanocrystalline CVO was performed according to our recent work[5] 3 μmol from a 0.05M solution of ligand-stripped Cu NCs in DMF were surface-oxidized in a vial by flowing oxygen for 15 min to form Cu@Cu_2O core@shell NCs. After this step, 3 μmol from a 0.05M stock solution of $VO(acac)_2$ in DMF were mixed with surface oxidized Cu NCs. The precursor solution (around 120μL) was drop casted on 1.5 cm x 1.5 cm substrates on a hot plate at 60°C in glove box. Annealing was carried out in air in a tube furnace at 350°C for 8 hours, preceded by 8°C min^{-1} heating ramp and followed by natural cooling.

Synthesis of the CVO/WO_3 nanocomposites.
For the nanocomposites, a precursor solution containing 3 μmol of Cu, 3 μmol of $VO(acac)_2$ and a varied amount of WO_3 in 210 μL DMF is prepared. To determine the amount of WO_3 to be added, it is assumed that all the Cu is converted to β-$Cu_2V_2O_7$ and thus, the film must contain 1.5 μmol of β-$Cu_2V_2O_7$. This corresponds to $5.11x10^{-4}$ g of β-$Cu_2V_2O_7$ and this mass is used to calculate the mass of WO_3 to be added in the precursor solution to obtain CVO/WO_3 with mass ratios of 1, 0.5 and 0.25. Thus, 2.2 μmol, 1.1 μmol and 0.55 μmol of WO_3 are added to form CVO/WO_3 with mass ratio of 1, 0.5 and 0.25, respectively. The precursor solution is then drop-casted on 1.5 cm x 1.5 cm substrates on a hot plate kept at 60°C. Annealing is performed in air in a tube furnace at 350°C for 8 hours, preceeded by 8°C min^{-1} heating ramp and followed by natural cooling.

Photoelectrochemical (PEC) characterization.
For the PEC characterization, 105 uL of precursor solution is deposited on 1.5 cm x 1.5 cm FTO substrates. The film thickness varies from around 350nm for the pure CVO up to around 600 nm for the 1:1 CVO/WO_3 nanocomposite. J-E curves were acquired in a typical three-electrode configuration using a SP-200 (BioLogic) potentiostat/galvanostat. The light source was an AM 1.5 solar simulator (ORIEL LCS-100 Series Solar Simulator model) with the illumination intensity adjusted to 100 mW/cm^2. All the illuminated areas were approximately 0.8 cm^2. The electrolyte was a sodium borate buffer solution (pH 8.2) with 0.1 M sodium sulfite (Na_2SO_3) as a hole scavenger. Photocurrents were monitored while sweeping the potential to the positive direction at a scan rate of 10 mV/s. The data reported in this study are obtained in back-illumination, yet front illumination leads to very similar curves considering the electrodes are porous and thin. While all measurements were carried out using a Ag/AgCl (3.5M KCl) as the reference electrode, all results in this work are presented against the reversible hydrogen electrode (RHE) for ease of comparison with other papers that use electrolytes with different pH conditions. The conversion between potentials vs. Ag/AgCl and vs. RHE is performed using the following equation:

$$E(\text{vs. RHE}) = E(\text{vs. Ag/AgCl}) + E_{Ag/AgCl}(\text{reference}) + 0.0591V * pH$$

$$EAg/AgCl\ (\text{reference}) = 0.1976\ V \text{ vs. NHE at } 25\ °C$$

A set of 3 photoelectrodes was tested for each studied photoanode and the average values are reported.

Nanosecond Transient Absorption Spectroscopy

The ns-TAS measurements were recorded with a custom set-up (LP980, Edinburgh Instruments Ldt., UK) able to record dynamics in the μs time range. The samples were pumped with 355 nm excitation pulse (third harmonic of a Nd:YAG laser; Ekspla NT 342, 5 ns pulse duration, 10 Hz repetition rate). A shutter before the sample regulates the pump frequency on the sample at 5 Hz. The intensity of the pump beam was regulated with neutral density filter. The pulsed probe beam was generated with a Xenon arc lamp 150 W, ozone free. The probe beam transmitted through the sample and filtered through a monochromator placed after the sample (300 mm focal length, Czerny-Turner with Triple Grating Turret). The signal was detected with a photomultiplier detector PMT (Hamamatsu R928) equipped with 5 stage dynode chain for high current linearity and collected with an oscilloscope (Tektronik MDO 3022). A cut-off filter was used in the entrance of the monochromator to cut the scattered light. Each traces has been averaged on 300 shots for almost 1 h. All the TAS measurements have been corrected from the fluoresce background and the probe background.

SEM

SEM images were acquired on a FEI Teneo 200 FEG Analytical Scanning Electron Microscope using a beam energy of 5 keV.

TEM

TEM images were acquired on a FEI Tecnai Spirit using a beam energy of 200 kV, equipped with a Gatan camera. Nanocrystal samples were drop-casted from solution on a copper TEM grid (Ted Pella, Inc) prior to imaging. STEM-HAADF imaging, HRTEM and energy dispersive X-ray analysis (EDX) were performed on a FEI Tecnai Osiris transmission electron microscope at an accelerating voltage of 200 kV. This microscope is equipped with a high brightness X-FEG gun, silicon drift Super-X EDX detectors and a Bruker Esprit acquisition software. EDX maps of 512x512 pixels were acquired using a beam current of 630 pA and with a dwell time of 50 msec per pixel. Samples were prepared by scratching the nanocomposite film with an ultrathin carbon coated gold TEM grid prior to imaging.

UV-vis Spectroscopy

The transmission and reflectance measurements were recorded on a Perkin Elmer-Lambda 1050 UV/Vis/NIR Spectrophotometer with a D2(Deuterium) lamp for ultraviolet and a WI(halogen) lamp for the visible and infrared range. Measurements were performed with an integrating sphere. . Measurements were performed with an integrating sphere. The absorption coefficient used for the Tauc plot calculation has been calculated with the following formula: $\alpha=-\ln(T/100+R/100)/d$, where d is the film thickness measured by the profilometer (~500 nm). All the samples for these measurametns were deposited on quartz substrate.

Raman spectroscopy and PL measuraments.

Raman spectra were recorded using a confocal Raman microscope (Renishaw inVia Raman microscope) with a 532 nm laser source of maximum power of 45W. The measurements were performed with a 100x objective in the Raman microscope with 5% of laser power. The spectral positions were calibrated by the characteristic Si phonon peak at 520.7 cm-1. The photoluminescence measurements were performed on the same instrument equipped with a 450 nm laser.

XRD

X-ray diffraction data was acquired on a Bruker D8 Discover diffractometer with a non-monochromated Cu Kα source equipped with a Lynxeye 1-D detector. A corundum standard (NIST

1976b) was used as a reference to determine the instrumental broadening in order to estimate the size-induced broadening of XRD peaks.

In-situ Grazing-incidence diffraction

Grazing incidence X-ray diffraction experiments were performed at The European Synchrotron Research Facility BM01 SNBL using a custom heating stage. All measurements were carried out with an incident wavelength of 0.6897 Å, and patterns were acquired with a PILATUS2M detector. Details of the beamline and equipment have been described elsewhere.[6] For each sample, an initial alignment was performed to minimize the signal from the Si single crystal substrate. The incident angle was set usually between 1.5 and 2.5 degrees. The spot size was fixed at 0.5x0.5mm. After the alignment, data was acquired for 10s for the in-situ experiments, and 30s for ex-situ experiments. Temperature of the sample was measured at the surface using a K-type thermocouple. Heating was achieved by a NiCr wire embedded in a ceramic plate. The heating plate was placed on four springs and clamped from above with two thin ceramic bars to mitigate thermal dilatation of the substrate and heating plate itself. The base was mounted on the goniostat available at the beamline, and was constantly cooled with water.

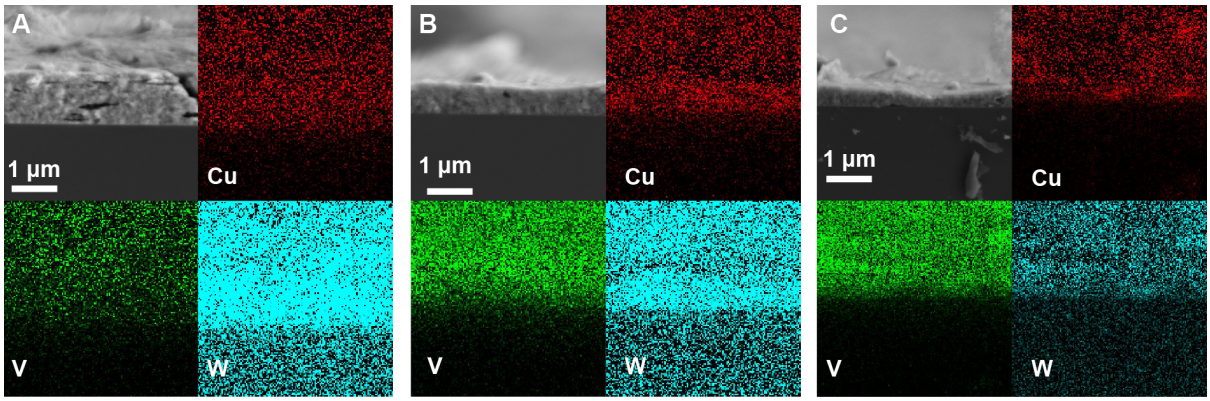

Figure S1: A-C) Cross-sectional SEM image of CVO/WO_3 = 1:1, CVO/WO_3 = 1:0.5 and CVO/WO_3 = 1:0.25 nanocomposite film along with the elemental EDX mapping. The overalapping of the W and Si peaks (S2,C) accounts for detection of W on the silicon substrate.

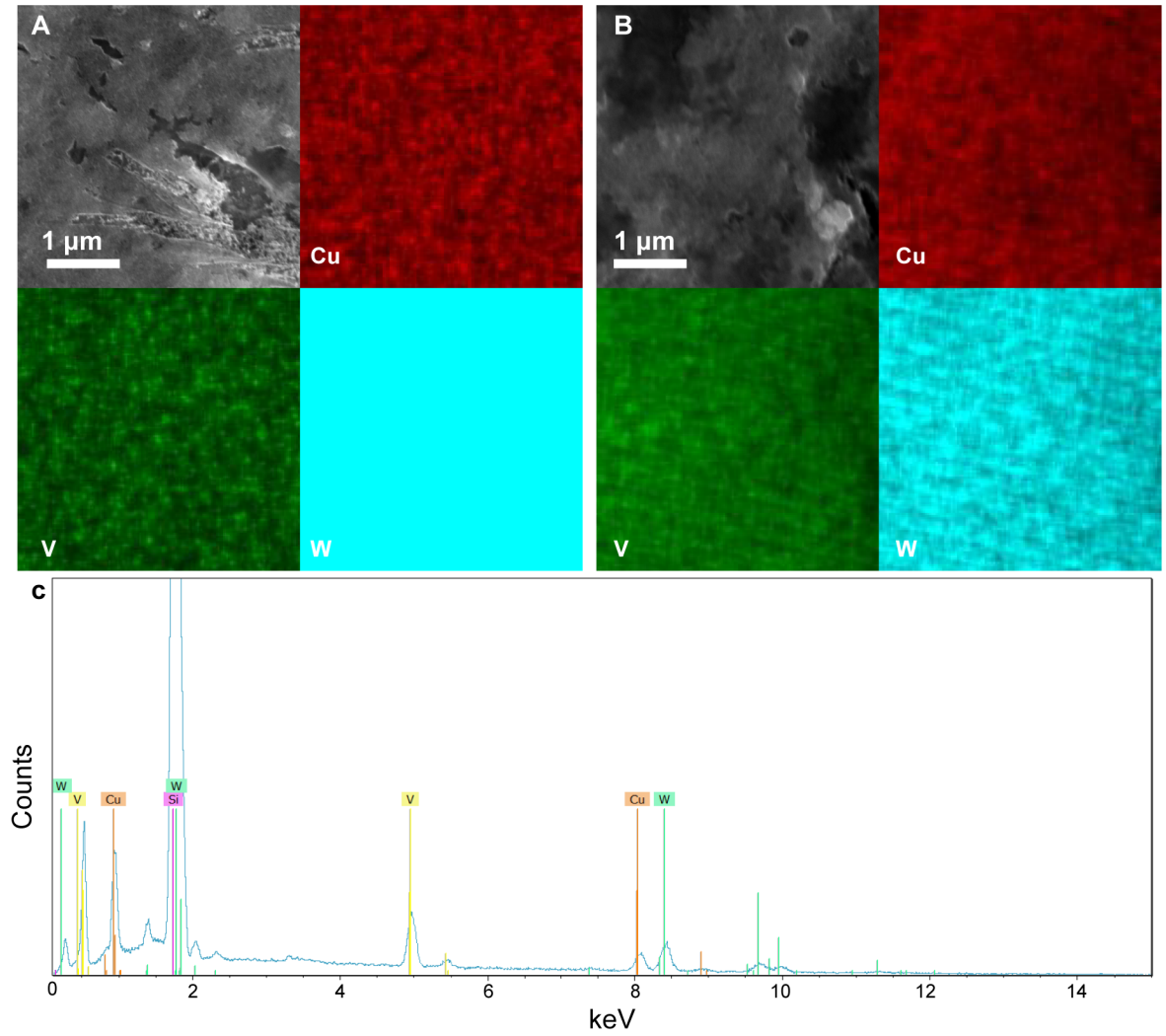

Figure S2: A,B) Top-view SEM image of CVO/WO_3 = 1:1 and CVO/WO_3 = 1:0.5 nanocomposite along with elemental EDX mapping. C) Typical EDX spectrum of CVO/WO_3=1:0.25 nanocomposite.

The quantification of V and W was not possible due to the overlap between the oxygen (0.52 eV) and vanadium (0.51 eV) peak positions as well as between silicon (1.74 eV) and tungsten (1.77 eV) peak positions.

Nanocomposite	Cu:V:W measured (at%)	CVO/WO_3 measured (wt%)	CVO/WO_3 expected (wt%)
CVO/WO_3=1:1	1:1:0.67	1:0.9	1:1
CVO/WO_3=1:0.5	1:1.5:0.3	1:0.42	1:0.5
CVO/WO_3=1:0.25	1:1.5:0.17	1:0.24	1:0.25

Table S1: ICP-OES elemental analysis of the nanocomposites films

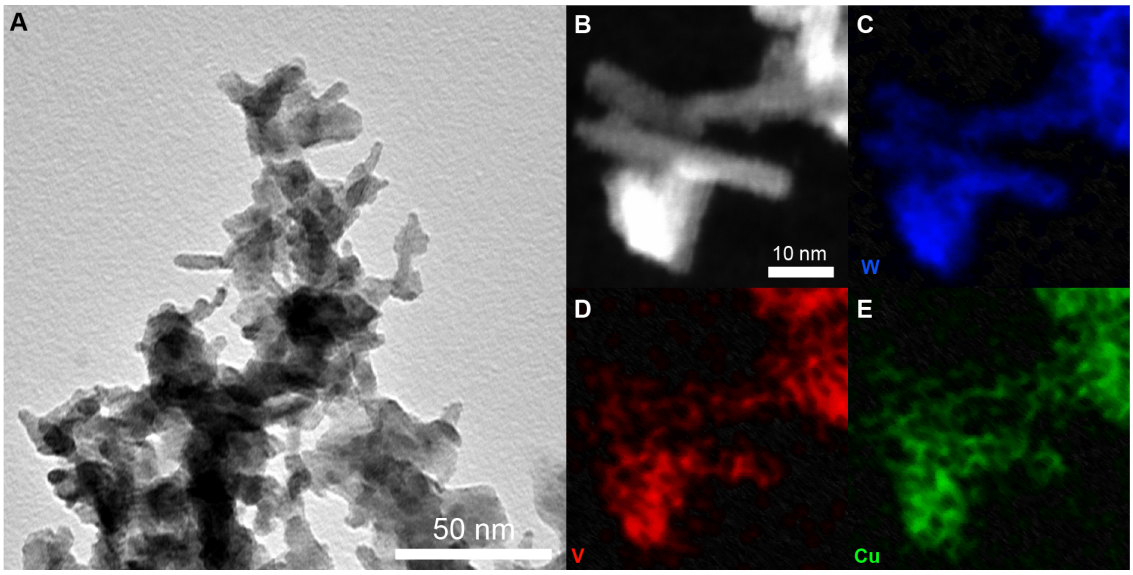

Figure S3. A) Low resolution TEM image of CVO/WO_3 nanocomposite with a ratio 1:0.25 showing the WO_3 nanorods embedded in the β-$Cu_2V_2O_7$. B) HAADF-STEM and C-E) corresponding EDX images of W, V and Cu respectively.

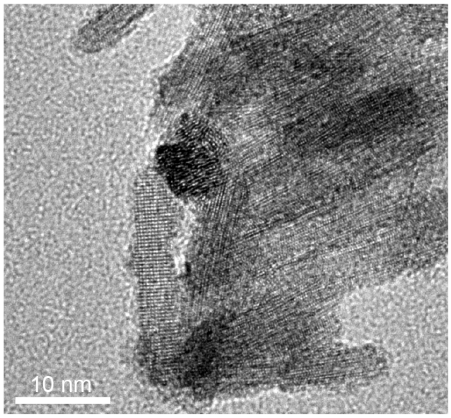

Figure S4. HR-TEM image of WO_3 nanorod annealed film showing no change in morphology after annealing, consistently with the preservation of peak width in the XRD patterns. It proves that the irregular shaped area on the nanorod showed in Figure 2B-C of the manuscript is not due to the annealing of the WO_3 nanorods but to the presence β-$Cu_2V_2O_7$.

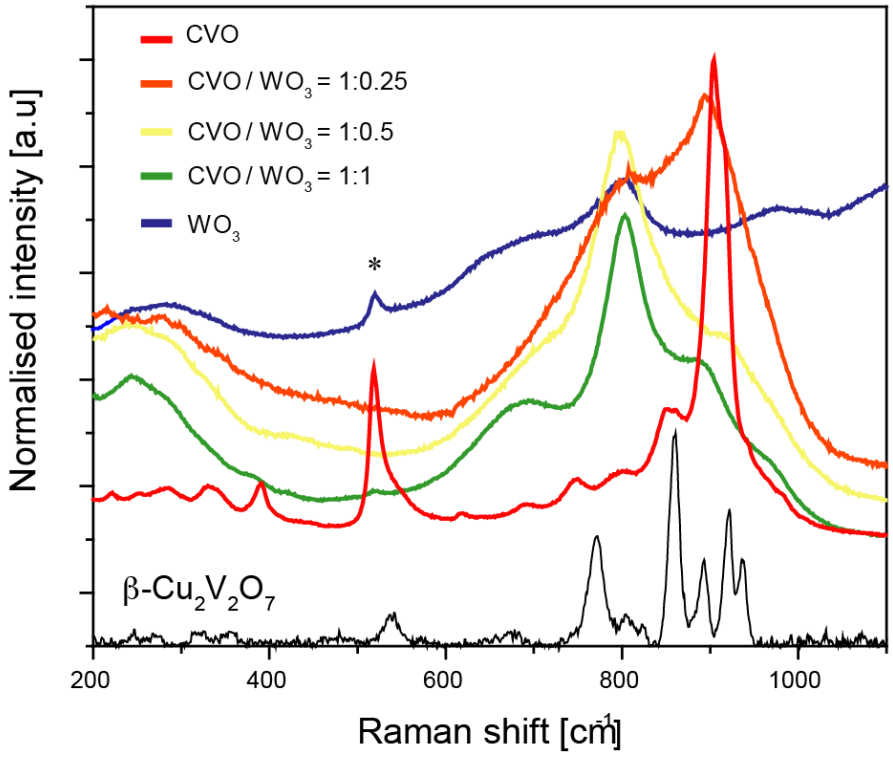

Figure S5: Raman spectra of WO_3, CVO/ WO_3 nanocomposites in different mass ratio (0.25 :1, 0.5:1 and 1:1) and CVO films. Reference spectra for β-$Cu_2V_2O_7$ is taken from RRUFF reference database (RRUFF ID: R070482). The signals corresponding to the Si substrate are indicated as * in the figure.

The presence of strongest modes of β–$Cu_2V_2O_7$ and WO_3 was used to determine the phase composition on the film. The broad scattering peak at 800 cm^{-1} , 680 cm^{-1} and 270 cm^{-1} correspond to the nanosized WO_3.[7] The scattering peaks at 903 cm^{-1}, 910 cm^{-1}, 860 cm^{-1}, 786 cm^{-1} and 389 cm^{-1} can be assigned to β–$Cu_2V_2O_7$ which is clearly seen in the CVO sample.[8] All the nano-composites have the peak at 800 cm^{-1} which can be assigned to WO_3 and the peak at 903 cm^{-1} which can be assigned to β–$Cu_2V_2O_7$. We observe an increase in the intensity of the WO_3 peak (800 cm^{-1}) with respect to the β–$Cu_2V_2O_7$ peak (903 cm^{-1}) with the increase in mass loading of WO_3 in the nanocomposites.

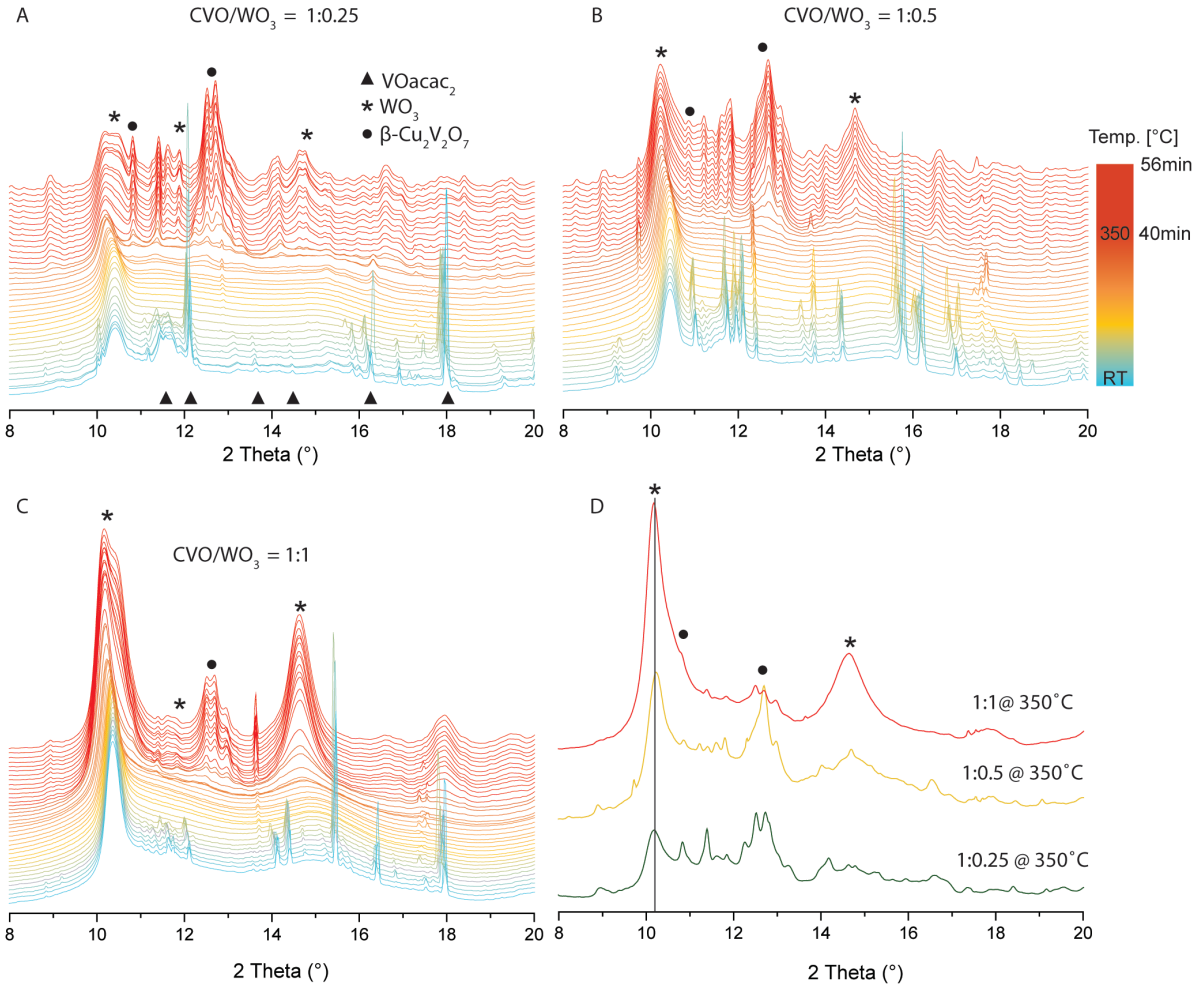

Figure S6: A, B, C) In-situ XRD measurements during the formation of CVO /WO_3 nanocomposites with different mass ratios. The initial scans reveal the presence of $WO_{2.72}$ and $VO(acac)_2$. Only WO_3 (*) and β–$Cu_2V_2O_7$(●) were observed in the final products. The same temperature scale is applicable to all the experiments. D) First patterns acquired after reaching 350°C during the in-situ experiments given for comparison with the ex-situ patterns.

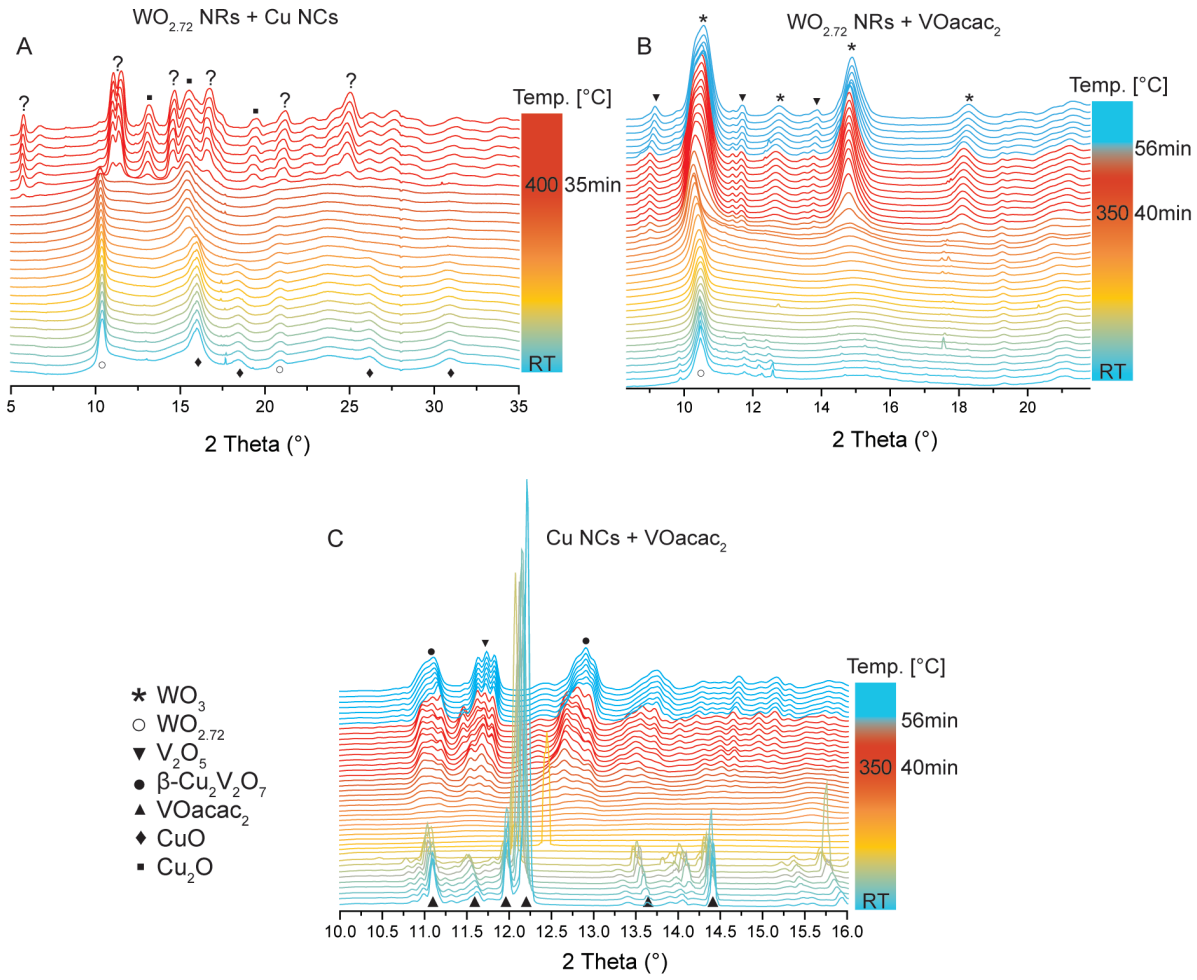

Figure S7: In-situ XRD measurements during the annealing of: A) $WO_{2.72}$ NRs + the surface oxidized Cu NCs ($Cu@Cu_2O$ NCs), B) $WO_{2.72}$ NRs + $VO(acac)_2$, C) the surface oxidized Cu NCs ($Cu@Cu_2O$ NCs) + $VO(acac)_2$. The heating profile is shown to the right of each figure.

These experiments were performed to assess the reactivities in the binary mixture even at a temperature higher than the 350°C utilized for the synthesis of nanocomposites. For the $WO_{2.72}$ NRs + $Cu@Cu_2O$ NCs mixture (Figure S5A) no modification is observed up to 350°C, consistently with the ex-situ data; at around 400°C we observe a drastic phase change with the appearance of new peaks. However, the product could not be assigned to any W-Cu-O compounds in the PDF database. For the $WO_{2.72}$ NRs + $VO(acac)_2$ mixture (Figure S5B) no interaction between the two phases is detected, and only pure WO_3 and V_2O_5 are identified in the final product even at temperatures above 350°C. Finally, for the Cu NCs + $VO(acac)_2$ mixture (Figure S5C) β–$Cu_2V_2O_7$ is detected at the same temperature (270 °C) as in the composite samples, together with V_2O_5 impurities.

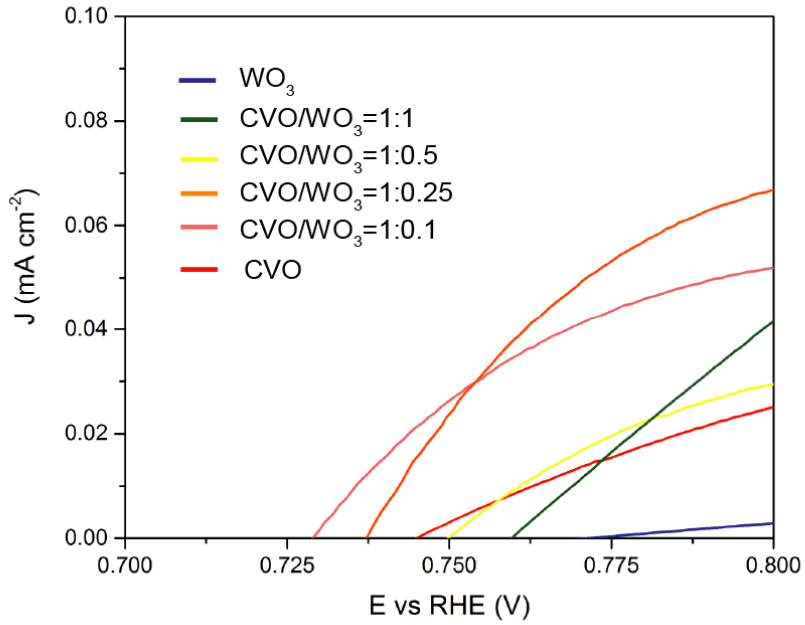

Figure S8. The onset potential of the nanocomposites in in a 0.1M sodium borate buffer (pH 8.2) containing 0.1M Na_2SO_3 as the hole scavenger using AM 1.5G (100 mW/cm^2) illumination.

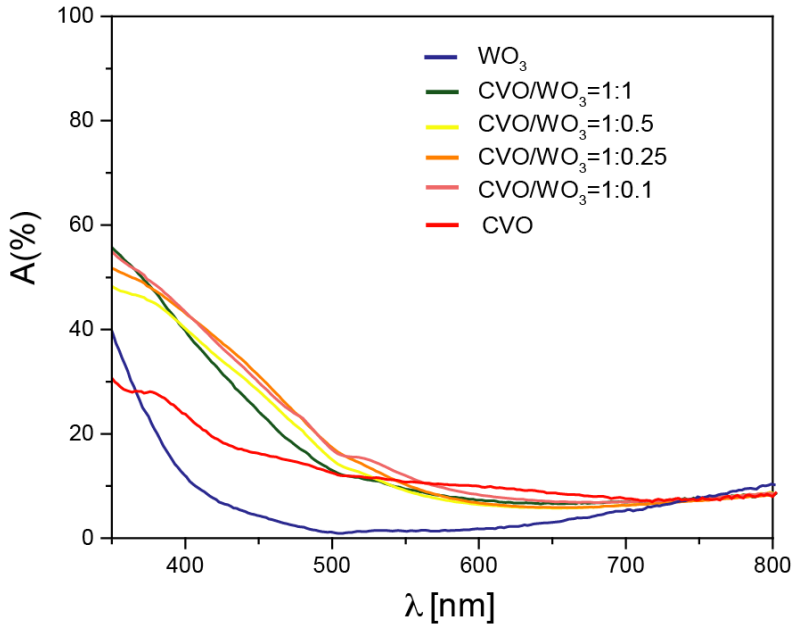

Figure S9. Optical absorption spectra of the pure WO_3, the pure CVO and the CVO/WO_3 nanocomposites in different mass ratio. These films were prepared on FTO for the PEC measurmanets and the data are shown without subtraction of FTO background. The reflectance (R(%)) and transmission (T(%)) of the films were measured using and integrating sphere, the optical absorption (%) was calculated from the formula $A(\%) = 100 - R(\%) - T(\%)$

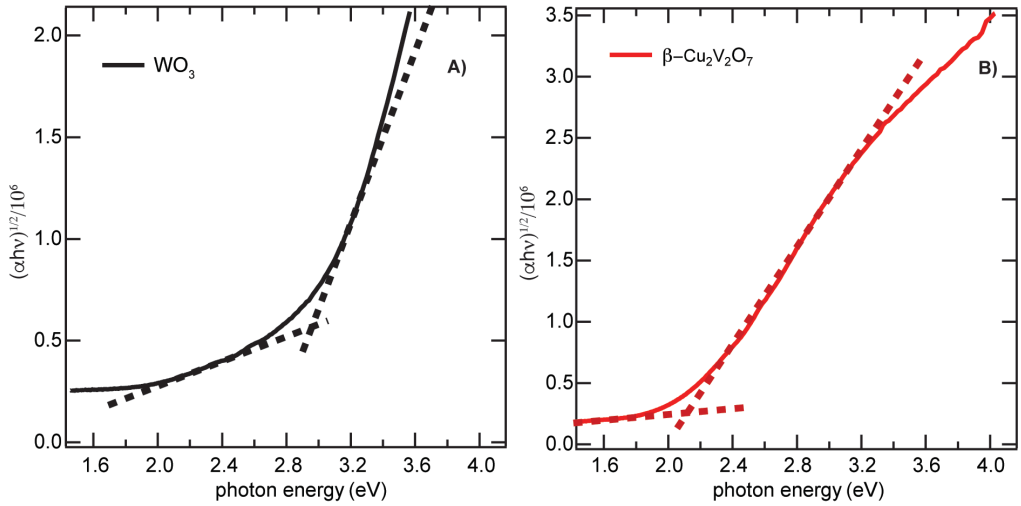

Figure S10: A) Tauc plots for the indirect transition of A) pure WO_3 B) pure B-$Cu_2V_2O_7$

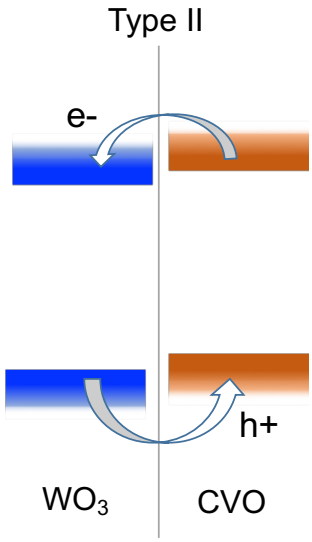

Considering the position of the onset potentials at 0.76 V and 0.74 V (Figure 4) and the band gaps of 2.9 eV and 2 eV (Figure S10) for WO_3 and β–$Cu_2V_2O_7$, respectively, the CBM of the WO_3 results 20 mV downshifted with respect to the CBM of the CVO. Here, the assumption that the onset potential corresponds to the flat band potential of the electrodes is made taking into account that the presence of the hole scavenger should reduce the kinetic limitation of charge transfer at the semiconductor/electrolyte interface. While this still remains an approximation, the experimental approach has already been followed and validated by Jae Sung Lee et al.[9] In addition, the photocurrent measurement for the best performing sample β–$Cu_2V_2O_7$/WO_3 = 1:0.1 presents a well-defined plateau (Figure 4), generally associated with enhanced charge generation efficiency.[10] Hence, we can conclude the formation of a type II junction is the most suitable of the two possibilities for explaining our findings.

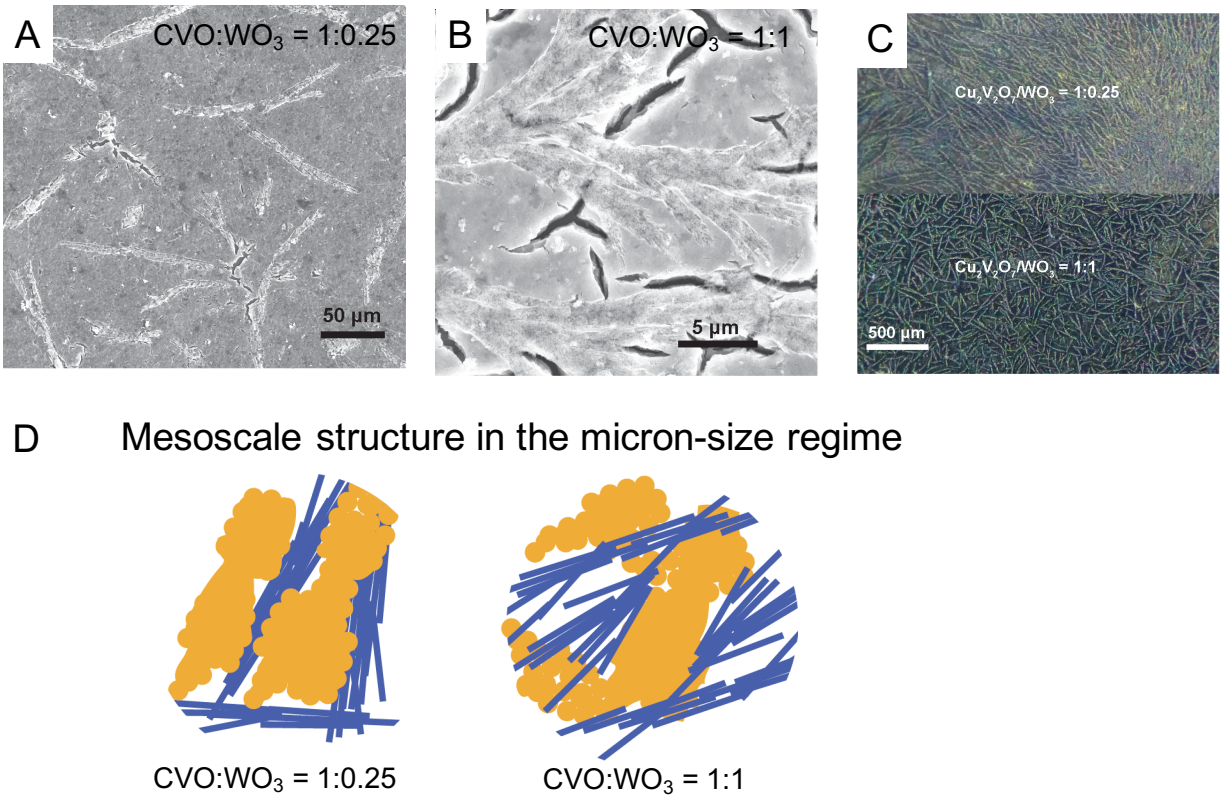

Figure S11: A,B) Low magnification top-down SEM images and C) optical microscopy images of the CVO/WO_3 nanocomposites 1:1 and 1:0.25. D) Illustration of the composition-dependent mesoscale structure induced by the nanoscale assembly of the Cu NCs and $WO_{2.7}$ NRs.

Interestingly, a composition-dependent micrometer-scale segregation is observed by low magnification SEM and optical microscopy. In the nanocomposites with CVO/WO_3 = 1:0.25 and 1:0.5 needle-shaped domains about 100 μm long can be identified (Figure S9A). With higher WO_3 loading in CVO/WO_3 = 1:1 nanocomposites, these needles turn into a continuous, hierarchical branching pattern on the surface of the films. Since this patterning is also present before the annealing, we propose that it might be due to ordered aggregation of the NRs during film deposition and solvent evaporation. While this ordered aggregation is detrimental in our case, it represents an interesting example of how nanoscale assembly impacts mesoscale structure in inorganic blends, in a similar manner in which the molecular interaction in organic bulk heterojunction impact the macroscale structure of the polymeric blends.[11-16]

REFERENCES

1 L.-I. Hung, C.-K. Tsung, W. Huang and P. Yang, *Adv. Mater.*, 2010, **22**, 1910–1914.

2 A. Loiudice, J. K. Cooper, L. H. Hess, T. M. Mattox, I. D. Sharp and R. Buonsanti, *Nano Lett.*, 2015, **15**, 7347–7354.

3 T. M. Mattox, A. Bergerud, A. Agrawal and D. J. Milliron, *Chem. Mater.*, 2014, **26**, 1779–1784.

4 E. L. Rosen, R. Buonsanti, A. Llordes, A. M. Sawvel, D. J. Milliron and B. A. Helms, *Angew. Chemie - Int. Ed.*, 2012, **51**, 684–689.

5 C. Gadiyar, M. Strach, P. Schouwink, A. Loiudice and R. Buonsanti, *Chem. Sci.*, , DOI:10.1039/C8SC01314D.

6 V. Dyadkin, P. Pattison, V. Dmitriev, D. Chernyshov and IUCr, *J. Synchrotron Radiat.*, 2016, **23**, 825–829.

7 M. Boulova and G. Lucazeau, *J. Solid State Chem.*, 2002, **167**, 425–434.

8 D. de Waal and C. Hutter, *Mater. Res. Bull.*, 1994, **29**, 843–849.

9 S. J. Hong, S. Lee, J. S. Jang and J. S. Lee, *Energy Environ. Sci.*, 2011, **4**, 1781.

10 A. J. Cowan and J. R. Durrant, *Chem. Soc. Rev.*, 2013, **42**, 2281–2293.

11 T.M. Clarke, J. R. Durrant, *Chem. Rev.*, 2010, **295**, 6736–6767.

12 W.U. Hyunh, J.J. Dittmer, A.P. Alivisatos , *Science*, 2002, **92**, 2425–2427.

13 B.M. Savoie, N.E. Jackson, L.X. Chen, T.J. Marks, M.A. Ratner, *Acc. Chem. Res.*, 2014, **47**, 3385–3394.

14 S. Weetnam,K.R. Graham,G.O. Ngongang Ndjawa, T. Heumüller, J.A. Bartelt, T.M. Burke, W. Li, W. You, A. Amassian, M.D. McGehee, *J. Am. Chem. Soc.*, 2014, **136**, 14078–14088.

15 J.A. Bartelt, J.D. Douglas, W.R. Mateker, A. El Labban, C.J. Tassone, M.F. Toney, J.M.J. Fréchet, P.M. Beaujuge, M.D. McGehee, *Adv. Energy Mater.*, 2014, **4**, 1301733.

16 S.M. Menke, A. Cheminal, P. Conaghan, N.A. Ran, N.C. Greehnam, G.C. Bazan, T.-Q. Nguyen, A. Rao, R. H. Friend, *Nature Comm.*, 2018, **8**, 277.